Impact of a Vertical Vorticity Constraint in Variational Dual-Doppler Wind Analysis: Tests with Real and Simulated Supercell Data

COREY K. POTVIN

NOAA/National Severe Storms Laboratory, Norman, Oklahoma

ALAN SHAPIRO AND MING XUE

School of Meteorology, and Center for the Analysis and Prediction of Storms, University of Oklahoma, Norman, Oklahoma

(Manuscript received 25 January 2011, in final form 23 August 2011)

ABSTRACT

One of the greatest challenges to dual-Doppler retrieval of the vertical wind is the lack of low-level divergence information available to the mass conservation constraint. This study examines the impact of a vertical vorticity equation constraint on vertical velocity retrievals when radar observations are lacking near the ground. The analysis proceeds in a three-dimensional variational data assimilation (3DVAR) framework with the anelastic form of the vertical vorticity equation imposed along with traditional data, mass conservation, and smoothness constraints. The technique is tested using emulated radial wind observations of a supercell storm simulated by the Advanced Regional Prediction System (ARPS), as well as real dual-Doppler observations of a supercell storm that occurred in Oklahoma on 8 May 2003. Special attention is given to procedures to evaluate the vorticity tendency term, including spatially variable advection correction and estimation of the intrinsic evolution. Volume scan times ranging from 5 min, typical of operational radar networks, down to 30 s, achievable by rapid-scan mobile radars, are considered. The vorticity constraint substantially improves the vertical velocity retrievals in our experiments, particularly for volume scan times smaller than 2 min.

1. Introduction

The vertical velocity (w) is the most poorly sampled wind component in typical (i.e., quasi horizontal) radar scanning geometries. Dual-Doppler analyses of w are therefore largely dependent on the horizontal divergence term in the mass conservation constraint. Because w is differentiated with respect to height in that constraint, it is necessary to impose one or more boundary conditions on w when the mass conservation equation is directly integrated. Even if the mass conservation equation is imposed in a 3DVAR framework (i.e., not directly integrated), use of a boundary condition on w can still improve the analysis (Shapiro et al. 2009, hereafter SPG09). The most obvious option is to impose the impermeability condition at the ground. However, radial velocity data, and thus information about low-level divergence, are often lacking near the surface due to earth curvature, nonzero base elevation angles, low signal-to-noise ratio, ground clutter contamination, beam blockage, and rough terrain. The resulting errors in the horizontal divergence estimated within the data gap can substantially degrade the analyzed w throughout the entire column.

In dual-Doppler analysis techniques in which horizontal divergence is explicitly integrated with height (the explicit integration approach), the horizontal divergence within the data gap is often set equal to some fraction of that at the lowest analysis level within the data column (e.g., Brandes 1977). Unfortunately, large errors in w throughout the column will occur in cases where the horizontal divergence field changes rapidly with height near the ground, which is a common scenario with convective storms. In the variational dual-Doppler analysis techniques, the solution for the wind field within the radar data gap can be obtained from mass conservation, smoothness, and background constraints, and so no

Corresponding author address: Dr. Corey K. Potvin, National Severe Storms Laboratory, National Weather Center, 120 David L. Boren Blvd., Norman, OK 73072.
E-mail: corey.potvin@noaa.gov

DOI: 10.1175/JTECH-D-11-00019.1

special treatment of the data gap is required (Gao et al. 1999). However, the w analyzed throughout the column may still contain large errors if the horizontal divergence field within the data gap is not accurately determined by these constraints alone.

Analysts often attempt to reduce these w errors as well as those that accumulate during integration of the mass conservation equation (in explicit integration techniques) by imposing the impermeability condition both at the ground and near the storm top. However, the resulting improvement in retrieved w can be severely limited (or reversed) by two factors. First, if dual-Doppler radar coverage terminates below the impermeability level, then the situation is analogous to that just described: lacking horizontal divergence information in the data gap creates potentially severe errors through the depth of the analysis domain. Second, even when dual-Doppler coverage extends up to the storm top (this frequently is not the case), the height at which w actually approaches zero is often highly uncertain, particularly if the storm is intensifying or decaying. Given these difficulties, imposing an upper-level boundary condition on w will often introduce errors as large as (or larger than) those resulting from using only a lower boundary condition.

A new mesoscale three-dimensional variational data assimilation (3DVAR) dual-Doppler analysis technique was developed by SPG09 that weakly (in a least squares sense) satisfies the anelastic vertical vorticity equation in addition to the data constraint, a mass conservation equation, and smoothness constraints. A series of data denial experiments was performed with analytical wind fields containing strong low-level convergence and divergence. When pseudo-observations were withheld near the surface, the vorticity constraint substantially improved retrievals of w. This finding is consistent with that of Liou and Chang (2009), who applied a very similar method to emulated dual-Doppler observations of a numerically simulated supercell pair. These results indicate that the vorticity equation can be used to improve retrievals of w in the common scenario where low-level data are lacking and the impermeability condition cannot be reliably imposed aloft. The potential role of the vertical vorticity equation in improving mesoscale dual-Doppler retrievals of the 3D wind field has also been examined in Protat and Zawadzki (2000), Protat et al. (2001), Mewes and Shapiro (2002), and Liu et al. (2005).

In the present study, the impact of the vorticity constraint is further explored using an Advanced Regional Prediction System (ARPS; Xue et al. 2000, 2001) simulation of a supercell thunderstorm, as well as real Doppler observations of a tornadic supercell that occurred in Oklahoma on 8 May 2003. Several improvements to the original SPG09 technique are described and their impacts on the analyses are examined. These modifications are primarily designed to better contend with unsteadiness in the observed flow.

Because of the characteristically long intervals (often 5 min) between radar volume scans in operational and even many research settings, direct fixed-frame computation of the local derivative of vorticity (by finite differencing the vorticity retrieved at a given location at two different times) can produce large discretization errors if portions of the wind field are rapidly moving or evolving. In SPG09 the local derivative was evaluated using a frozen turbulence space–time transformation that necessitates estimates of the wind field translation components U and V. Their experiments revealed that the success of the vorticity constraint can be significantly diminished (or even reversed) by large errors in these estimates. Given that the advection velocity field is often highly spatially inhomogeneous in the presence of vigorous convection, the use of spatially constant U and V in the vorticity constraint can presumably introduce significant errors into the analysis (especially of w). Thus, the present study uses a recently developed pattern translation retrieval method that allows for spatially variable U and V (Shapiro et al. 2010a,b). The use of spatially variable U and V also better conditions the data constraint, which uses these estimates to account for the translation of the wind field during the observational period. In Shapiro et al. (2010a,b), and in this study, the U and V characterize the advection of local reflectivity patterns.

Advection correction addresses only one source of wind field unsteadiness, namely, translation. Failure to account for the intrinsic evolution of the horizontal wind field between the analysis time and the observation collection times can also degrade the retrieval, especially in the presence of developing or decaying convection. In this study, we examine the impact of including estimates of the evolution of the horizontal wind components and vertical vorticity in the data and vorticity constraints, respectively. These estimates are obtained from two provisional wind retrievals performed prior to the final dual-Doppler analysis. We are especially interested in the impact of the vorticity evolution estimates because large errors in the local vorticity tendency term can significantly limit the utility of the vorticity constraint.

The rest of this paper is organized as follows. The updated analysis procedure is described in section 2. Experiments with pseudo-observations generated from the high-resolution ARPS supercell simulation are presented in section 3. Retrievals of the 8 May 2003 Oklahoma supercell are presented in section 4. A summary and recommendations for future work follow in section 5.

2. Methodology

a. Updated cost function formulation

As in SPG09, the analyzed Cartesian wind components $u^a(x, y, z)$, $v^a(x, y, z)$, and $w^a(x, y, z)$ are obtained in this study by minimizing a cost function J that quantifies violations of data, mass conservation, vorticity, and smoothness constraints. Unlike in SPG09, however, J is modified in some of our experiments to include precalculated estimates of the intrinsic evolution of the horizontal wind and/or vertical vorticity fields. These estimates are computed from provisional dual-Doppler analyses of two consecutive volume scans.

The calculation of the modified J is now described, with details of the provisional dual-Doppler analyses and estimation of the wind field translation and evolution deferred until sections 2b,c. As in the original approach,

$$J = J_O + J_M + J_V + J_S, \tag{1}$$

where J_O, J_M, J_V, and J_S are the cost functions associated with the observational, mass, conservation, vorticity, and smoothness constraints, respectively. In each of these cost functions, the (constant) constraint weight is represented by a subscripted λ. The observational cost function

$$J_O \equiv \sum_{\text{Rad1}} \lambda_{O1}(v_{r1}^{\text{obs}} - v_{r1}^{a})^2 + \sum_{\text{Rad2}} \lambda_{O2}(v_{r2}^{\text{obs}} - v_{r2}^{a})^2 \tag{2}$$

sums the root-mean-square (RMS) differences between the observed and analyzed radial winds over the observational spaces of two radars, Rad1 and Rad2 (although the formulation could easily be extended to three or more radars). The spatial coordinates of the radial wind observations (v_{r1}^{obs} and v_{r2}^{obs}) are transformed from the spherical radar grid to the Cartesian analysis space. Because the analyzed velocity vectors (whose radial projections are labeled v_{r1}^{obs} and v_{r2}^{obs}) are valid at a single analysis time ($t = 0$) while the observations are valid over a period during which the wind field may change substantially, it may be beneficial to correct for the translation and intrinsic evolution of the wind field in the evaluation of J_O. To account for the translation of the wind field between $t = 0$ and the collection time t^* of an observation at (x^*, y^*, z^*), the analyzed radial wind is computed from the u^a, v^a, and w^a evaluated at the backward-shifted location given by

$$(x, y, z) = [x^* - U(x^*, y^*, z^*)t^*, y^* - V(x^*, y^*, z^*)t^*, z^*], \tag{3}$$

where U and V are the precalculated advection velocity components. Note that the U and V fields represent the motion of a geometrical pattern (reflectivity in this case), and not necessarily true air parcel velocities (see section 3 of Shapiro et al. 2010a). In some experiments, precalculated pattern-following u and v tendencies, Du/Dt and Dv/Dt, are used to account for intrinsic evolution of the horizontal wind field between the analysis and observation times. The horizontal wind evolution estimates and analyzed wind components are interpolated to the shifted locations (x, y, z) using an isotropic 3D Cressman (1959) method. The analyzed radial wind for radar n ($n = 1$ or 2) is calculated as

$$v_{r_n}^{a} = \mathbf{r}_n(x^*, y^*, z^*) \cdot \left\{ \begin{array}{l} \mathbf{i}\left[u^a(x, y, z) - t\dfrac{Du}{Dt}(x, y, z)\right] \\ + \mathbf{j}\left[v^a(x, y, z) - t\dfrac{Dv}{Dt}(x, y, z)\right] \\ + \mathbf{k}[w^a(x, y, z) - |w_t|] \end{array} \right\}, \tag{4}$$

where w_t is the estimated terminal velocity of hydrometeors relative to the air (e.g., Shapiro et al. 1995), and

$$\mathbf{r}_n(x^*, y^*, z^*) = (\cos\theta \sin\phi)\mathbf{i} + (\cos\theta \cos\phi)\mathbf{j} + (\sin\theta)\mathbf{k}$$

is the radial unit vector for the azimuth angle ϕ and elevation angle θ of the radar beam.

The anelastic mass conservation cost function is unchanged from SPG09 and is expressed by

$$J_M \equiv \sum_{\text{Cart}} \lambda_M \left[\frac{\partial u^a}{\partial x} + \frac{\partial v^a}{\partial y} + \frac{\partial w^a}{\partial z} + \frac{w^a}{\rho}\frac{\partial \rho}{\partial z}\right]^2, \tag{5}$$

where the base-state atmospheric density $\rho_s(z)$ profile is assumed in this study to be $\rho_s(z) = \rho_0 \exp(-z/H)$ with reference density $\rho_o = 1$ kg m^{-3} and scale height $H =$ 10 km. This and the remaining cost functions are computed over the Cartesian analysis grid (Cart).

The anelastic vertical vorticity equation used in the analysis procedure is

$$\frac{\partial \zeta}{\partial t} + \mathbf{u} \cdot \nabla\zeta + \left(\frac{\partial v}{\partial z}\frac{\partial w}{\partial x} - \frac{\partial u}{\partial z}\frac{\partial w}{\partial y}\right) + \zeta\left(\frac{\partial u}{\partial x} + \frac{\partial v}{\partial y}\right) = 0, \tag{6}$$

where the vertical vorticity $\zeta \equiv \partial v/\partial x - \partial u/\partial y$ and $\mathbf{u}$ is the 3D wind vector. Justification for the use of this approximated vorticity equation is given in SPG09. For volume scan time intervals (hereafter, volume scan times) that are characteristic of current operational and research radars, we generally do not seek to compute the local vorticity derivative directly because this may introduce large temporal discretization errors (see section

3d). Instead, consider the total vorticity derivative in the pattern-following reference frame used in (3),

$$\frac{D\zeta}{Dt} = \frac{\partial \zeta}{\partial t} + \mathbf{U} \cdot \nabla \zeta, \tag{7}$$

where $\mathbf{U} \equiv U\mathbf{i} + V\mathbf{j}$ is the horizontal advection velocity. Rearranging terms, we can write the local vorticity derivative as the sum of an intrinsic evolution term and a translation term

$$\frac{\partial \zeta}{\partial t} = \frac{D\zeta}{Dt} - \mathbf{U} \cdot \nabla \zeta. \tag{8}$$

Substituting for the local derivative in (6), we obtain

$$\frac{D\zeta}{Dt} + (\mathbf{u} - \mathbf{U}) \cdot \nabla \zeta + \left(\frac{\partial v}{\partial z}\frac{\partial w}{\partial x} - \frac{\partial u}{\partial z}\frac{\partial w}{\partial y}\right) + \zeta\left(\frac{\partial u}{\partial x} + \frac{\partial v}{\partial y}\right) = 0. \tag{9}$$

In SPG09, only the contribution of the wind field translation to the local vorticity tendency was considered; that is, $D\zeta/Dt$ was implicitly set to zero. In the present study, however, we will make provision for $D\zeta/Dt$ (using the same approach used to account for evolution of the horizontal wind field). The new vorticity constraint can therefore be expressed as

$$J_V \equiv \sum_{\text{Cart}} \lambda_V \left[\frac{D\zeta}{Dt} + (u^a - U)\frac{\partial \zeta^a}{\partial x} + (v^a - V)\frac{\partial \zeta^a}{\partial y} + w^a\frac{\partial \zeta^a}{\partial z} + \left(\frac{\partial v^a}{\partial z}\frac{\partial w^a}{\partial x} - \frac{\partial u^a}{\partial z}\frac{\partial w^a}{\partial y}\right) + \zeta^a\left(\frac{\partial u^a}{\partial x} + \frac{\partial v^a}{\partial y}\right)\right]^2. \tag{10}$$

Finally, the smoothness cost function is modified from SPG09 to use second-order rather than first-order spatial derivatives

$$J_S \equiv \sum_{\text{Cart}} \lambda_{S1}\left[\left(\frac{\partial^2 u^a}{\partial x^2}\right)^2 + \left(\frac{\partial^2 u^a}{\partial y^2}\right)^2 + \left(\frac{\partial^2 v^a}{\partial x^2}\right)^2 + \left(\frac{\partial^2 v^a}{\partial y^2}\right)^2\right] + \sum_{\text{Cart}} \lambda_{S2}\left[\left(\frac{\partial^2 u^a}{\partial z^2}\right)^2 + \left(\frac{\partial^2 v^a}{\partial z^2}\right)^2\right] + \sum_{\text{Cart}} \lambda_{S3} \times \left[\left(\frac{\partial^2 w^a}{\partial x^2}\right)^2 + \left(\frac{\partial^2 w^a}{\partial y^2}\right)^2\right] + \sum_{\text{Cart}} \lambda_{S4}\left(\frac{\partial^2 w^a}{\partial z^2}\right)^2. \tag{11}$$

Whether first- or second-order derivatives are used, J_S penalizes small-scale noise in the analyzed wind field and spreads observational information into data voids. Using second-order derivatives allows spatial trends in the wind field to be extended into regions of missing data. The potential advantages and disadvantages of first- and second-order smoothing are discussed in SPG09. Although it is not clear a priori whether one option is generally preferable to the other, both produced similar RMS errors in our preliminary analyses (not shown).

Most first-order spatial derivatives in the procedure are calculated using two-point centered finite differences valid over 2Δ, where Δ is the (isotropic) analysis grid spacing. The exception is the vertical mass flux term in the mass conservation equation, which is computed over Δz using ρ, w at vertically adjacent analysis levels. The stenciling of our flux divergence term is thus patterned after that used in the popular Custom Editing and Display of Reduced Information in Cartesian Space (CEDRIC; Mohr et al. 1986) software. Second-order spatial derivatives of velocity components in the vorticity equation are computed as successive first-order finite differences. In contrast, the second-order derivatives in the smoothness constraint are computed using three-point centered differences that are valid over 2Δ.

The values of the cost function weights determine the relative influence of each of the constraints in the analysis. Each weight is expressed as the product of a nondimensional tuning parameter and a normalization factor designed to narrow the tuning parameter space that must be explored when determining the optimal tuning parameter values. The normalization process has been modified from that presented in SPG09.

The observational constraint weight for a radial velocity observation collected by radar n is normalized by the ratio of the local number of radial velocity observations collected by radar n to the local number of analysis points. This ratio $M^{\text{local}}/N^{\text{local}}$ is calculated within 2Δ of each observation and is designed to allow the observational constraint to have as much influence within sparsely sampled regions (e.g., at large ranges from the radar) as in densely sampled regions. The cost function weights are given by

$$\lambda_{On} = C_O\left\{\left(\frac{M^{\text{local}}}{N^{\text{local}}}\right)\frac{1}{M_1 + M_2}\left[\sum_{\text{Rad1}} (v_{r1}^{\text{obs}})^2 + \sum_{\text{Rad2}} (v_{r2}^{\text{obs}})^2\right]\right\}^{-1}, \quad n = 1 \quad \text{or} \quad 2 \tag{12}$$

$$\lambda_M = C_M[(A)^2]^{-1}, \tag{13}$$

$$\lambda_V = C_V[(A)^4]^{-1}, \quad \text{and} \tag{14}$$

$$\lambda_S = C_S[(B)^2]^{-1}, \tag{15}$$

where

$$A \equiv \left\{ \frac{1}{M_1 + M_2} \left[\sum_{\text{Rad1}} \left(\frac{1}{r_1} \frac{\partial v_{r1}^{\text{obs}}}{\partial \theta} \right)^2 + \sum_{\text{Rad2}} \left(\frac{1}{r_2} \frac{\partial v_{r2}^{\text{obs}}}{\partial \theta} \right)^2 \right] \right\}^{1/2}, \quad (16)$$

$$B \equiv \left\{ \frac{1}{M_1 + M_2} \left[\sum_{\text{Rad1}} \left(\frac{1}{r_1} \frac{\partial^2 v_{r1}^{\text{obs}}}{\partial \theta^2} \right)^2 + \sum_{\text{Rad2}} \left(\frac{1}{r_2} \frac{\partial^2 v_{r2}^{\text{obs}}}{\partial \theta^2} \right)^2 \right] \right\}^{1/2}, \quad (17)$$

M_1 and M_2 are the total numbers of analyzed observations from each radar, and the tuning parameters are denoted by subscripted Cs.[1] We set $C_{O1} = C_{O2} = C_O$ and $C_{S1} = C_{S2} = C_{S3} = C_{S4} = C_S$.

The analysis (control) variables $u^a(x, y, z)$, $v^a(x, y, z)$, and $w^a(x, y, z)$ are obtained by minimizing J using the Polak–Ribiere conjugate gradient method (Press et al. 1992). A first guess of zero is used for all the control variables. With every ten iterations of the minimization procedure, the updated control variables are compared with their values from the tenth prior iteration. The procedure is considered to have converged once the change in u (in provisional retrievals, described in section 2c) or w (in final retrievals) is less than 0.02 m s^{-1} everywhere.

b. Advection correction

In severe convective storms the advection velocity field can be highly spatially variable, with features in different locations (e.g., left- and right-moving supercell pair) or with different scales (e.g., tornado revolving within a mesocyclone), often translating at very different velocities. Thus, in this study, the pattern translation velocity is estimated using a recently developed advection correction method that makes provision for spatially variable translation components $U(x, y, z)$ and $V(x, y, z)$ (Shapiro et al. 2010a,b). The method is designed to operate on constant-height or constant–elevation angle analyses of reflectivity or radial velocity that are valid at two different times. The retrieved U, V at each vertical analysis level weakly satisfies the frozen turbulence hypothesis and a smoothness constraint.

In our experiments, the advection retrieval procedure was applied to constant altitude plan position indicator (CAPPI) analyses of reflectivity (from one radar) that were valid at each of the analysis levels for two consecutive volume scans (volumes 1 and 2, or volumes 2 and 3). Reflectivity values <0 dBZ were rejected to emulate the lack of reflectivity data in regions of low signal-to-noise ratio. The final dual-Doppler analyses are valid at $t = 0$, which corresponds to the beginning of volume 1. The volumes 2 and 3 scans begin at $t = T$ and $t = 2T$, respectively, where T is the period between successive volume scans. Two sets of advection velocity components are thus retrieved: U_1, V_1, which are valid from $t = 0$ to $t = T$, and U_2, V_2, which are valid from $t = T$ to $t = 2T$. The space–time correction (3) used in the data and vorticity constraints is therefore valid to the extent that Taylor's (1938) frozen turbulence hypothesis is satisfied by the observed reflectivity fields, and the reflectivity is a passive tracer of the airflow. Although U and V were allowed to vary both along a trajectory and between trajectories in the advection retrieval, we do not account for variations in U and V along individual trajectories in (3). However, the loss of accuracy is minimal because these variations will typically be small due to the smoothness of the U, V fields.

c. Provisional retrievals and evolution correction

The evolution estimates for the horizontal velocity components Du/Dt, Dv/Dt used in (4) and the vorticity field $D\zeta/Dt$ used in (9) are calculated from two provisional horizontal wind retrievals valid at the beginnings of volume 1 (u_1, v_1) and volume 2 (u_2, v_2). The provisional retrieval is obtained by minimizing the same cost function J defined in (1), but without the vorticity constraint ($J_V = 0$) because preliminary experiments (not shown) suggested that u and v are well retrieved just using the observational, mass conservation, and smoothness constraints.[2] The vertical vorticity fields ζ_1 and ζ_2 are computed from the two provisional horizontal wind fields.

To calculate the evolution terms, the positions of hypothetical parcels located at each of the analysis grid points at the beginning of volume 1 (x_1, y_1, z_1, 0) are tracked to the beginning of volume 2 as follows: (x', y', z') = ($x_1 + U_1{*}T, y_1 + V_1{*}T, z_1$). The estimated u, v, and ζ for each parcel at $t = T$ (u', v', and ζ') are then

[1] The ARPS experiments in section 3 used a slightly different normalization procedure for λ_{On} in which M^{local} was the number of local observations collected by both radars, not just by radar n. Because the emulated radars in those experiments were positioned equidistantly from the analysis domain, it was expected that using the less refined normalization would have little impact. This was verified in a set of experiments (not shown) in which the differences in the velocity components retrieved using the two normalization procedures were generally <0.1 m s^{-1}.

[2] In preliminary provisional wind retrievals with the vorticity constraint included, w^a (which does not get used in the final dual-Doppler analyses) was improved, but at the expense of slightly degraded u^a and v^a.

interpolated from the u_2, v_2, and ζ_2 fields. The evolution estimates are next calculated as

$$Du/Dt(x_1, y_1, z_1) = (u' - u_1)/T,$$
$$Dv/Dt(x_1, y_1, z_1) = (v' - v_1)/T,$$
$$D\zeta/Dt(x_1, y_1, z_1) = (\zeta' - \zeta_1)/T. \quad (18)$$

Finally, a seven-point 3D smoother (with the central point assigned twice as much weight as the two neighboring points in each dimension) is applied to the fields to mitigate noise.

Inevitably, some air parcels located within the final analysis domain at $t = 0$ will be outside that domain when they are sampled by the radar. To make the greatest use of available radar data, then, it is necessary to estimate U and V at some observational locations that lie outside the final analysis domain. We therefore use a provisional domain that extends beyond the lateral boundaries of the final analysis domain in our experiments to ensure that U and V are calculated near all of the observations that get used in the final retrieval. Another advantage of using a provisional domain that encloses the final analysis domain is that it permits the calculation of the evolution terms (18) in cases where u' and v' are valid outside of the final analysis domain.

The dual-Doppler analysis methods developed in Protat and Zawadzki (2000), Liu et al. (2005), and Liou and Chang (2009) also account for unsteadiness in the horizontal wind and vorticity fields. In those approaches, the analyzed radial winds within the retrieval period (two successive volume scans) are assumed to vary linearly in time. The wind fields at two time levels are simultaneously retrieved using observational, mass conservation, and vorticity (among other) constraints, with the temporal (local) vorticity derivative expressed in terms of those two wind fields. In Liu et al. (2005) and Liou and Chang (2009), the temporal vorticity derivative is evaluated in the fixed frame. Our approach and that of Protat and Zawadzki (2000) also acknowledge the potential value of using velocity data from successive volume scans in the data constraint and in the evaluation of the temporal vorticity derivative. However, rather than imposing a linear-in-time assumption directly (fixed frame) within the vorticity constraint, these last two methods impose it in a pattern-following framework to mitigate the severe errors that may result if advection effects are not taken into account.

3. Experiments with ARPS supercell simulation

a. ARPS simulation and radar emulation

The impact of the vorticity constraint was tested using a very high-resolution ARPS simulation of a supercell (also used by Xue et al. 2007; Liu et al. 2007; May et al. 2007; Potvin et al. 2009). This facilitated verification of analyses (because the true u, v, and w fields are known) while providing a more realistic test of the technique than the analytical wind fields used in SPG09. The model thunderstorm was initiated by a thermal bubble placed in a homogeneous environment defined by a sounding proximate to the 20 May 1977 Del City, Oklahoma, supercell storm (Ray et al. 1981). Computations were performed over a 48 km × 48 km × 16 km domain with 25-m horizontal grid spacing and vertical grid spacing increasing from 20 m at the surface to about 80 m at 1 km above ground level (AGL) to 380 m at 16 km AGL. Time splitting was used to integrate acoustic waves on a finer temporal scale (0.04 s) than was used in the other processes (0.125 s). The simulation proceeded in a translating reference frame chosen to maintain the parent storm near the domain center throughout the simulation. The Kessler-type warm rain microphysics was used. The model fields used in our retrieval experiments begin 3.5 h into the simulation. The simulated storm exhibits many commonly observed supercell features, including a mesocyclone and an associated strong central updraft, a hooklike signature in the emulated reflectivity field, and a rear-flank downdraft (Fig. 1).

The provisional dual-Doppler analyses and advection velocity retrieval proceeded over the lowest 6 km of a 36 km × 36 km × 16 km subdomain of the ARPS simulation. The final dual-Doppler analyses were performed over a 20 km × 20 km × 6 km subdomain of the provisional domain (Fig. 2). The reasons for adopting a final analysis domain that is embedded within the provisional domain were discussed in section 2c. Both domains have 500-m grid spacing in all three dimensions. The lower-left corner of the provisional domain is the origin of the Cartesian coordinate system used in these experiments.

Emulated radars at ($x = -7.5$ km, $y = -13$ km, $z = 0$ km) and ($x = 42.5$ km, $y = -13$ km, $z = 0$ km) scanned volume sectors that spanned ~90° in azimuth and elevation angles from 0.5° to 21.5°. Observations were emulated at range, azimuthal, and elevational intervals of 200 m, 1°, and 1°, respectively. The volume scan time varied between our experiments from 30 s to 5 min, making the results relevant to dual-Doppler analyses of data from both rapidly scanning radars, such as the Doppler on Wheels (DOW; Wurman et al. 1997), and more conventional radars like the Weather Surveillance Radar-1988 Doppler (WSR-88D).

Radar observations were emulated using ARPS data that were provided at 5-s intervals. Observations along a radial at time t^* were generated using the ARPS data that were valid at the simulation time between t^* and

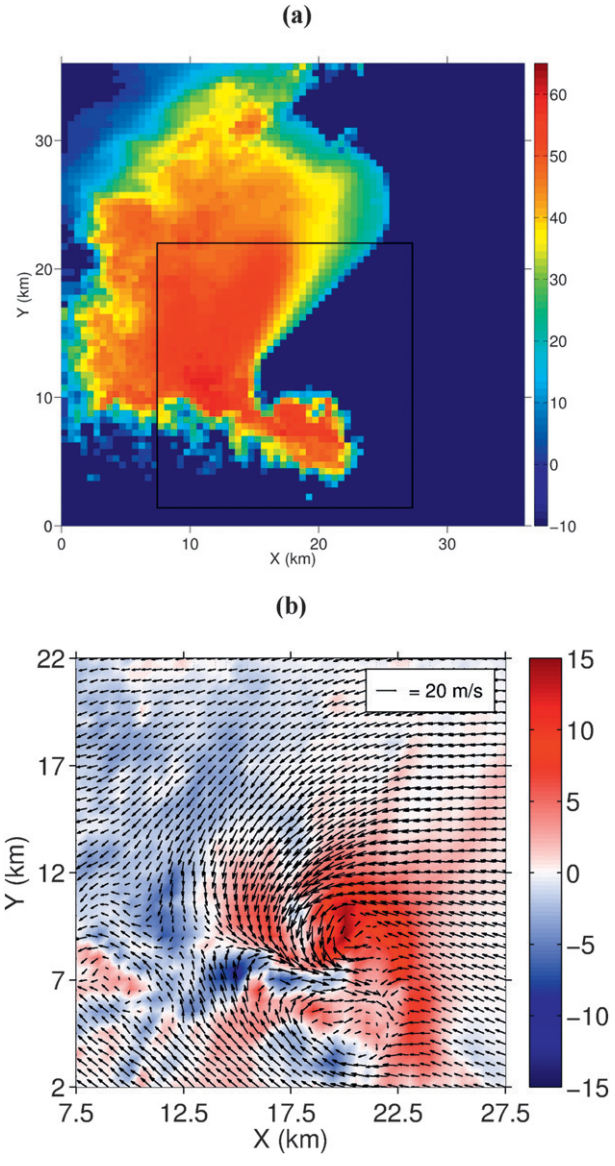

FIG. 1. Selected ARPS-simulated fields at $t = 0$, $z = 1$ km: (a) reflectivity (dBZ) and horizontal wind vectors over the provisional dual-Doppler analysis domain, and (b) vertical velocity (m s^{-1}) and horizontal wind vectors over the final horizontal dual-Doppler analysis domain, represented by the box in (a).

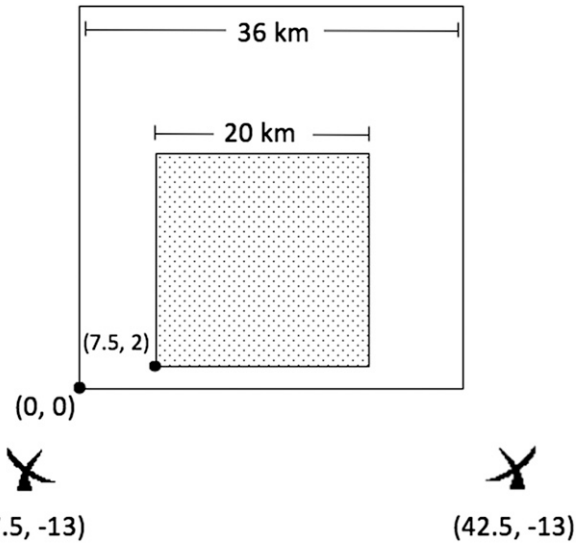

FIG. 2. The final and provisional analysis domains and relative radar locations in the ARPS experiments.

$t^* - 5$ s. The emulated radial velocity observations were generated by Cressman interpolating (cutoff radius = 500 m) the ARPS u, v, and w values on the 25-m grid to the spherical radar grid and calculating the corresponding radial projection. Reflectivity pseudo-observations were computed using the same interpolation procedure. The reflectivity (dBZ) values R were calculated by

$$R = 10\log\left[\frac{10^{18} \times 720(\rho q_r)^{1.75}}{\pi^{1.75} N_r^{0.75} \rho_r^{1.75}}\right] \quad (19)$$

(Tong and Xue 2005), where N_r is the rainfall drop size distribution intercept parameter (the Marshall–Palmer $N_r = 8.0 \times 10^6$ m^{-4} is used in this study), ρ is the air density (1 kg m^{-3}), ρ_r is the rainwater density (1000 kg m^{-3}), and q_r is the model rainwater mixing ratio vertically interpolated to the analysis grid.

b. Experimental setup and verification

Three main types of retrievals were performed to explore the impact of the vorticity constraint: CONTROL, NOVORT, and VORT. In all three types, the data, mass conservation, and smoothness constraints were weakly imposed (i.e., least squares error), and the impermeability condition was exactly satisfied at the ground. The impermeability condition was not imposed at storm top because this can be problematic in practice (for the reasons given in section 1). In the CONTROL experiments, all of the pseudo-observations were used. In the default NOVORT and VORT experiments, radial velocities lying below a data cutoff height $z = 1.5$ km were omitted from the provisional and final retrievals. In a separate set of experiments, the data cutoff height was alternately set to $z = 0$, 0.5, and 1 km. The vorticity constraint was weakly imposed in the VORT experiments but was not imposed in the NOVORT or CONTROL experiments. In the NOVORT and VORT experiments, Du/Dt, Dv/Dt, and $D\zeta/Dt$ were set to zero at and below the data cutoff height; and U, V below the data cutoff height were set equal to the U, V at the data cutoff height. The U, V retrievals used a smoothness weighting coefficient $\beta = 200$ dBZ^2 and a computational time step $\Delta t = 15$ s (Shapiro et al. 2010a). The retrieved U, V were visually

confirmed to be consistent with displacements of reflectivity features that were evident on CAPPIs valid at successive times.

The u, v, and w fields used to verify the dual-Doppler analyses were generated by upscaling the ARPS wind components to the analysis grid scale using Cressman interpolation. A 500-m cutoff radius was used to generate u and v, while a 1000-m cutoff radius was used to generate w (the vertical profile of which is shown in Fig. 3) because w^a should be approximately valid on the horizontal scale of the discretized 2D divergence used in the mass conservation constraint. The RMS errors in u^a, v^a, and w^a were calculated for each analysis level. Only analysis points located within 500 m of an emulated radial velocity observation (prior to the rejection of data below 1.5 km) from each radar, and collocated with $R \geq 5$ dBZ, were used in the RMS error calculations.

The tunable constraint weighting parameters were optimized for each experiment type by trial and error. The following set of weights was used in most of the ARPS experiments: $C_O = 1$, $C_M = 30$, $C_S = 10^{-4}$, and (in the VORT experiments) $C_V = 10^{-4}$. The only exception was that $C_M = 1$ in experiments with no data cutoff (e.g., CONTROL), although the differences between CONTROL analyses performed using the two C_M values were relatively minor. A 750-m Cressman radius was used in the interpolation of horizontal wind evolution estimates and analyzed wind components to the backward-shifted locations given by (3) in the data constraint. Because the ARPS wind components represent air motion, not particle motion, w_t was set to zero in (4) in these experiments.

c. *Preliminary CONTROL and NOVORT experiments: Correcting for flow unsteadiness*

Preliminary tests of this 3DVAR formulation focused on the CONTROL and NOVORT experiments. In this section, we explore the impact of correcting for wind field advection and evolution in the data constraint. Experiments are labeled with suffixes indicating the type of flow correction: -N (no flow correction), -A (advection correction), -E (evolution correction), or -AE (both advection and evolution correction).

In CONTROL-A and NOVORT-A with $T = 30$ s and $T = 2$ min, RMS errors in u^a, v^a decreased by ~2%–10% (relative to CONTROL-N and NOVORT-N) at higher levels of the domain, and increased by 1%–2% at lower levels. When T was increased to 5 min, the data advection correction reduced RMS errors in u^a, v^a by 2%–10%. The largest improvements occurred near the top of the domain in all cases, consistent with the tendency for displacements of wind field features between the observational and analysis times to increase with height.

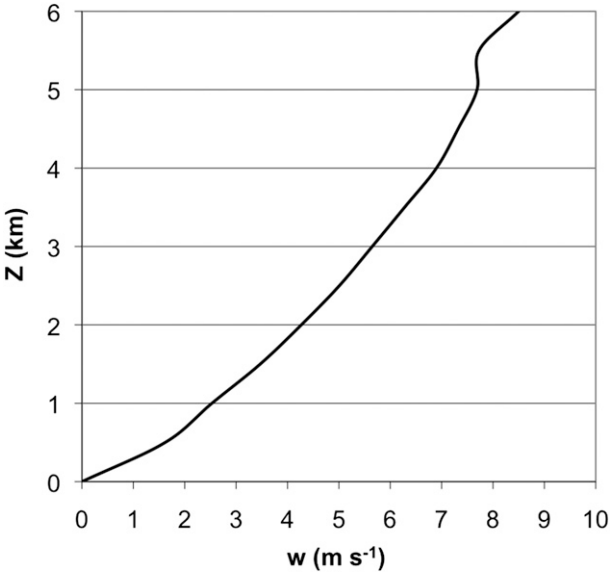

FIG. 3. The RMS (over the horizontal domain) upscaled ARPS ("true") w at each analysis level.

The mild degradation of u^a, v^a for $T = 30$ s and 2 min can be explained as follows. The retrieved U, V fields were qualitatively consistent with the displacement of the ARPS wind fields between $t = 0$ and $t = T$ (not shown). The U, V were relatively small (generally 5–10 m s^{-1}) because the ARPS simulation was performed in a moving reference frame chosen to follow the storm. Given the shorter periods between the observational and analysis times at lower elevation angles and the relatively small U, V, it is plausible that any minor improvements gained in u^a, v^a at lower levels by accounting for the displacement of the wind field were offset by interpolation errors. For $T = 5$ min, on the other hand, the improvement from accounting for the larger wind field displacement outweighed the interpolation errors, which do not increase with T. The RMS errors in w^a generally differed by <1% between NOVORT-A and NOVORT-N. Larger differences, however, occurred between CONTROL-A and CONTROL-N, in which the data advection correction reduced errors in w^a by up to 5% (10%) for $T = 2$ min ($T = 5$ min).

In CONTROL-E and NOVORT-E, u^a, v^a errors at lower levels decreased by 1%–3% relative to CONTROL-N and NOVORT-N for all T. The impact of the evolution correction on u^a, v^a at higher levels was more dependent upon T, with mild error reductions (1%–3%) occurring for $T = 5$ min but with errors increasing by 1%–3% (2%–10%) for $T = 2$ min ($T = 30$ s). As with the data advection correction, using evolution correction in NOVORT had little impact on w^a (errors generally changed by <1% between NOVORT-E and

NOVORT-N). The effect of evolution correction on w^a in the CONTROL experiments, however, was somewhat more significant. Errors in w^a in CONTROL-E changed by <1% (relative to CONTROL-N) at all levels for $T = 30$ s, increased by up to 10% at higher levels for $T = 2$ min, and decreased (increased) by up to 5% at lower (higher) levels for $T = 5$ min.

Errors in u^a, v^a in NOVORT-AE generally decreased relative to those in NOVORT-A by 1%–2% at lower levels and increased by 3%–6% at higher levels for $T = 30$ s. Errors in u^a, v^a generally increased by 2%–5% for $T = 2$ min. Errors generally increased by 0%–2% at lower levels and decreased by 1%–3% at higher levels for $T = 5$ min. The differences in the u^a, v^a errors between CONTROL-AE and CONTROL-A were similar to those between NOVORT-AE and NOVORT-A above the 1.5-km data cutoff height in the NOVORT experiments. Below 1.5 km, the u^a, v^a errors were generally 1%–3% lower in CONTROL-AE than in CONTROL-A. Errors in w^a in NOVORT-AE were generally 1%–2% larger than in NOVORT-A at lower levels and 1%–2% larger (smaller) at upper levels in the $T = 5$ min ($T = 30$ s and $T = 2$ min) retrievals. The w^a errors in CONTROL-AE generally differed from those in CONTROL-A by < 1% for $T = 30$ s, decreased by ~1% at lower levels and increased by ~5%–10% at higher levels for $T = 2$ min, and decreased (increased) by ~1%–3% at lower (higher) levels for $T = 5$ min.

Because the horizontal wind evolution correction did not generally improve the CONTROL and NOVORT retrievals, it was not included in most of the experiments shown in this paper. Errors in the evolution estimates may have resulted from advection correction errors in the provisional retrievals and from nonlinear evolution of the ARPS horizontal wind field. Fortunately, the data advection correction had a net positive impact on the retrievals, particularly at higher analysis levels and for larger T. This correction was thus used in all subsequent (including VORT) experiments presented in this paper (for convenience, the -A suffix is hereafter omitted from the experiment labels).

d. Impact of vorticity constraint

In the experiments with a 1.5-km data cutoff height, including the vorticity constraint in the dual-Doppler analysis procedure reduced the RMS w^a error for all T (Fig. 4), with the greatest improvements occurring near the middle ($z = 3$ km) of the analysis domain. The reduction in RMS w^a error at $z = 3$ km in the VORT analyses relative to the NOVORT analyses was 33%, 28%, 27%, and 19% for the 30-s, 1-min, 2-min, and 5-min retrievals, respectively. That the 5-min VORT retrieval was superior to the 30-s NOVORT retrieval

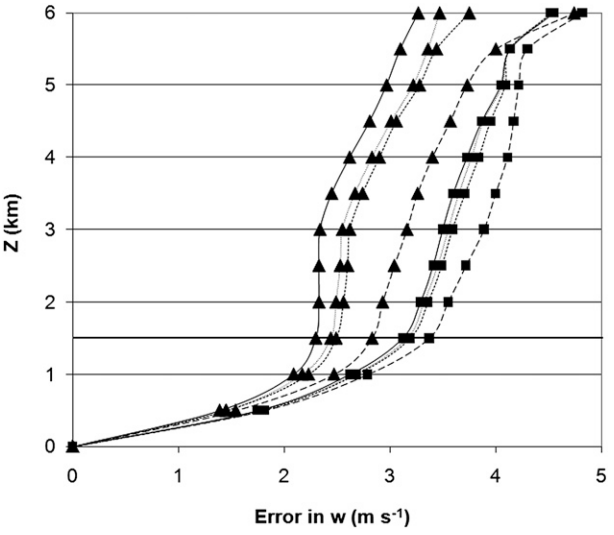

FIG. 4. The RMS w^a error in VORT (triangles) and NOVORT (squares) for $T = 30$ s (solid curves), 1 min (dotted curves), 2 min (short-dashed curves), and 5 min (long-dashed curves). The bold horizontal line represents the 1.5-km data cutoff height.

highlights both the potentially significant impact of missing low-level data on vertical velocity analyses and the utility of the vorticity constraint in mitigating the resulting errors. Horizontal and vertical cross sections of w^a reveal that the vorticity constraint produced the greatest improvement within the stronger updrafts (Fig. 5). The vorticity constraint had very little impact on u^a and v^a above the data void (Fig. 6) because these are already well determined by the remaining constraints.

Several variants of the VORT experiment were performed to examine the effects of accounting for the advection and evolution of the vorticity field: VORT-neither, VORT-adv, and VORT-direct (Fig. 7). In the VORT-neither retrievals, the advection and evolution terms were set to zero, and so $\partial\zeta/\partial t = 0$. In the VORT-adv retrievals, $D\zeta/Dt = 0$. In the VORT-direct retrievals, $\partial\zeta/\partial t$ was calculated as an Eulerian derivative (i.e., in the fixed reference frame) from two provisional retrievals in which data advection correction was not used.

Setting $\partial\zeta/\partial t = 0$ (VORT-neither) substantially diminished the utility of the vorticity constraint for all T. Not surprisingly, directly evaluating $\partial\zeta/\partial t$ (VORT-direct) worked well for $T = 30$ s (even producing slightly better results than the VORT retrieval), but was disadvantageous for larger T because of increasing temporal discretization errors. Repeating the VORT-direct experiments, but with data advection correction performed in the provisional retrievals (i.e., accounting for vorticity evolution, but not vorticity advection), produced very slight improvement in w^a (not shown). The $T = 5$ min VORT-adv retrieval was actually slightly more accurate

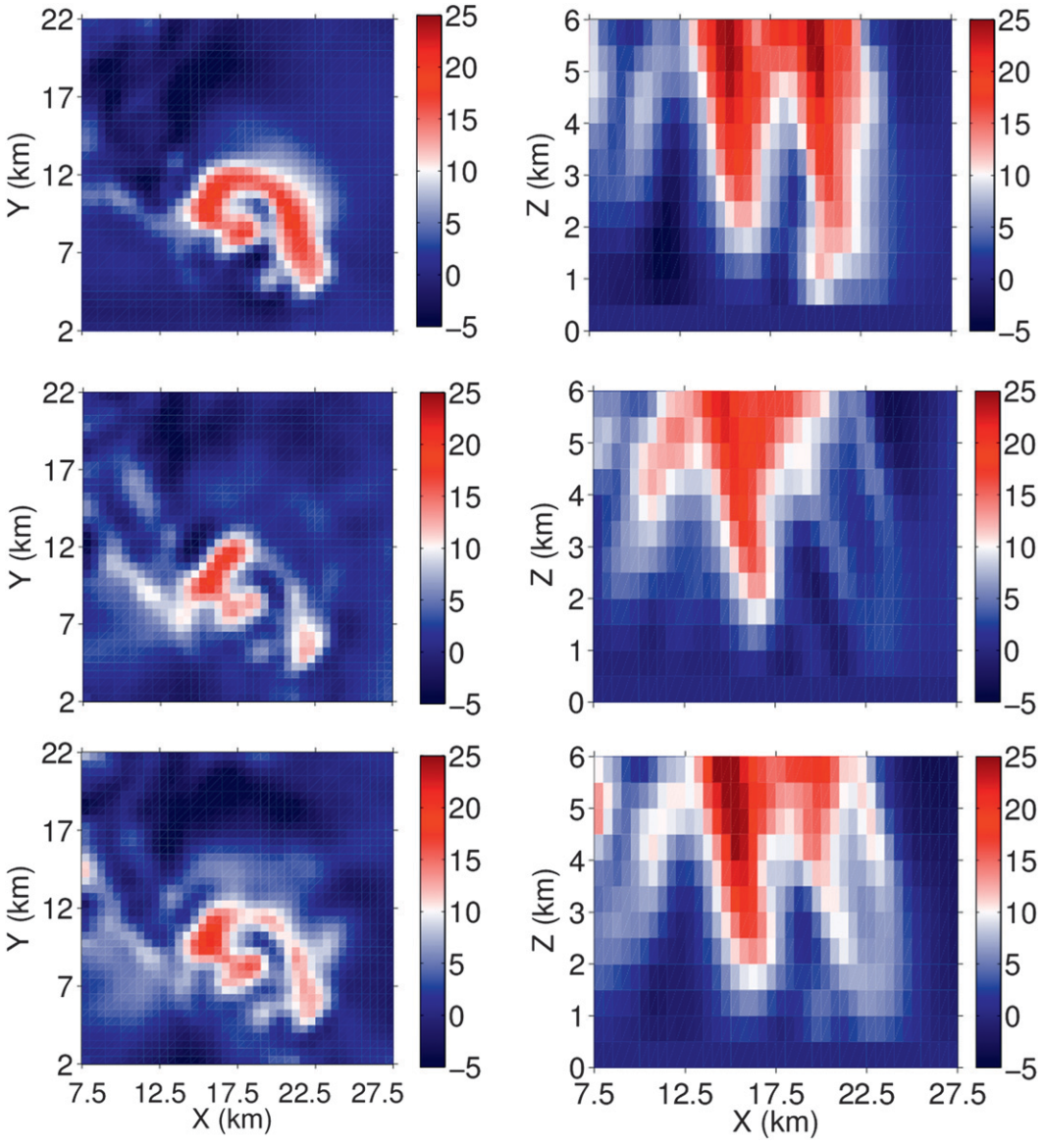

FIG. 5. (top) "True" w, (middle) NOVORT w^a, and (bottom) VORT w^a for $T = 2$ min at (left) $z = 3$ km and (right) $y = 10$ km.

than the $T = 5$ min VORT retrieval. This is because the benefit of accounting for evolution (in addition to advection) of the vorticity field diminished with increasing T resulting from errors in the calculation of $D\zeta/Dt$. Thus, it may be prudent to set $D\zeta/Dt = 0$ for very large T, although it should be noted that the value of T beyond which the evolution term becomes problematic may be highly case dependent. Since accounting for both advection and evolution of the vorticity field generally produced the best results in these experiments, both terms were used in the remaining VORT experiments discussed in this section.

Differences between the absolute errors in the NOVORT and VORT-adv w^a fields were visually compared to the upscaled ARPS w and ζ to identify possible scenarios in which the vorticity constraint may fail to improve w^a (Fig. 8). Fortunately, within the convectively active region of the storm, the vorticity constraint generally improved w^a, regardless of whether the collocated vorticity was large. In areas outside the main updraft/downdraft region of the storm, however, the impact of the vorticity constraint was as often favorable as unfavorable. It may therefore be desirable to restrict the application of the vorticity constraint to regions of the storm where

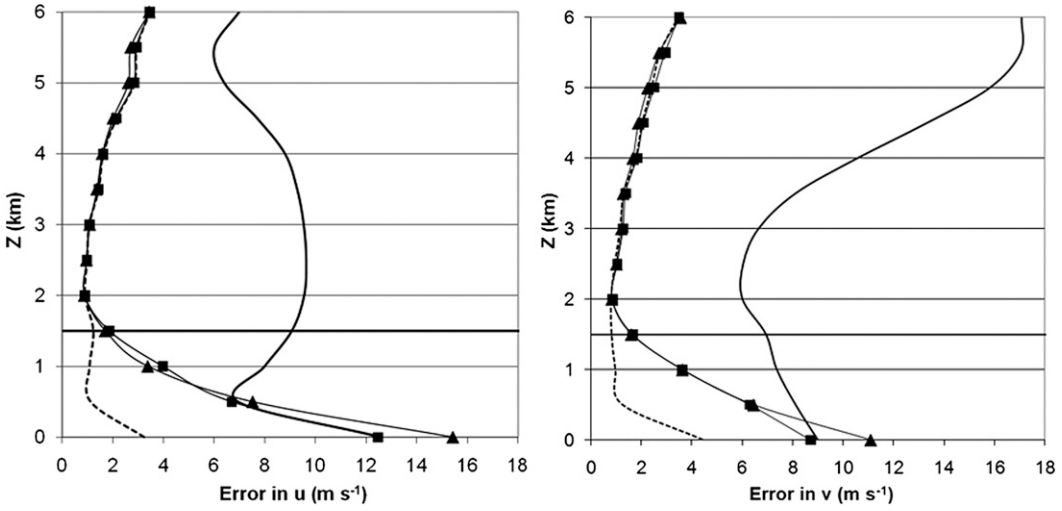

FIG. 6. The RMS errors in (left) u^a and (right) v^a in the $T = 2$ min CONTROL (dashed curves), NOVORT (squares), and VORT (triangles) retrievals. The plain curves indicate the "true" u and v. The bold horizontal line represents the 1.5-km data cutoff height.

the magnitude of w is assumed (e.g., based on the w^a obtained in the provisional retrievals) to exceed a particular threshold.

To evaluate the impact of the vorticity constraint for different low-level radar data coverage scenarios, a set of $T = 2$ min retrievals was performed in which the data cutoff height was incrementally decreased to $z = 0$ m (Figs. 9 and 10). In some of these experiments (Fig. 10), radial velocities collocated with reflectivity <5 dBZ were also withheld from the analysis to emulate the effect of low signal-to-noise ratios on velocity data coverage. As expected, the impact of the vorticity constraint diminished as the low-level data coverage (and accompanying information about the low-level divergence field) increased. When all of the radial wind data were included in the analysis, the vorticity constraint had a slightly negative impact on the retrieval. This is consistent with the expectation that the vorticity constraint will tend to be more substantially violated than the data and mass conservation constraints because of errors in $\partial\zeta/\partial t$ as well as potentially large discretization errors in the second-order spatial derivative terms. In all cases where some of the radial wind data were withheld from the analysis, however, the vorticity constraint substantially improved the w^a. For example, when the reflectivity threshold was imposed, the VORT retrieval with data omitted below $z = 1.5$ km was better than the NOVORT retrieval with data omitted below $z = 0.5$ km.

That the VORT retrieval with no data cutoff was superior to the CONTROL retrieval when the reflectivity threshold was imposed is very significant (Fig. 10). This result arises in part from the severe degradation of the CONTROL retrieval when the reflectivity threshold was imposed. This suggests that low-reflectivity regions beneath storms can substantially degrade retrievals of w even when the radars observe very close to the ground. Fortunately, the vorticity constraint in this case reduced the RMS w^a errors (relative to the NOVORT retrieval) by 10%–22% above $z = 0.5$ km. In additional experiments with $T = 30$ s, $T = 1$ min, and $T = 5$ min (not shown), RMS w^a errors were reduced by 12%–23%, 14%–26%, and 0%–10%, respectively, above $z = 0.5$ km. Most of the improvement occurred near the eastern edge of the updraft region, which was roughly collocated with the 5-dBZ reflectivity contour. Some improvement was also noted near and just above the weak echo region of the storm.

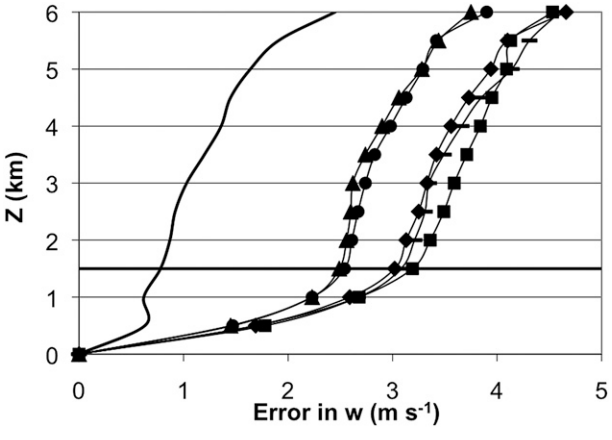

FIG. 7. The RMS w^a errors in CONTROL (plain curve), NOVORT (squares), VORT (triangles), VORT-neither (diamonds), VORT-adv (circles), and VORT-direct (dashes) for $T = 2$ min.

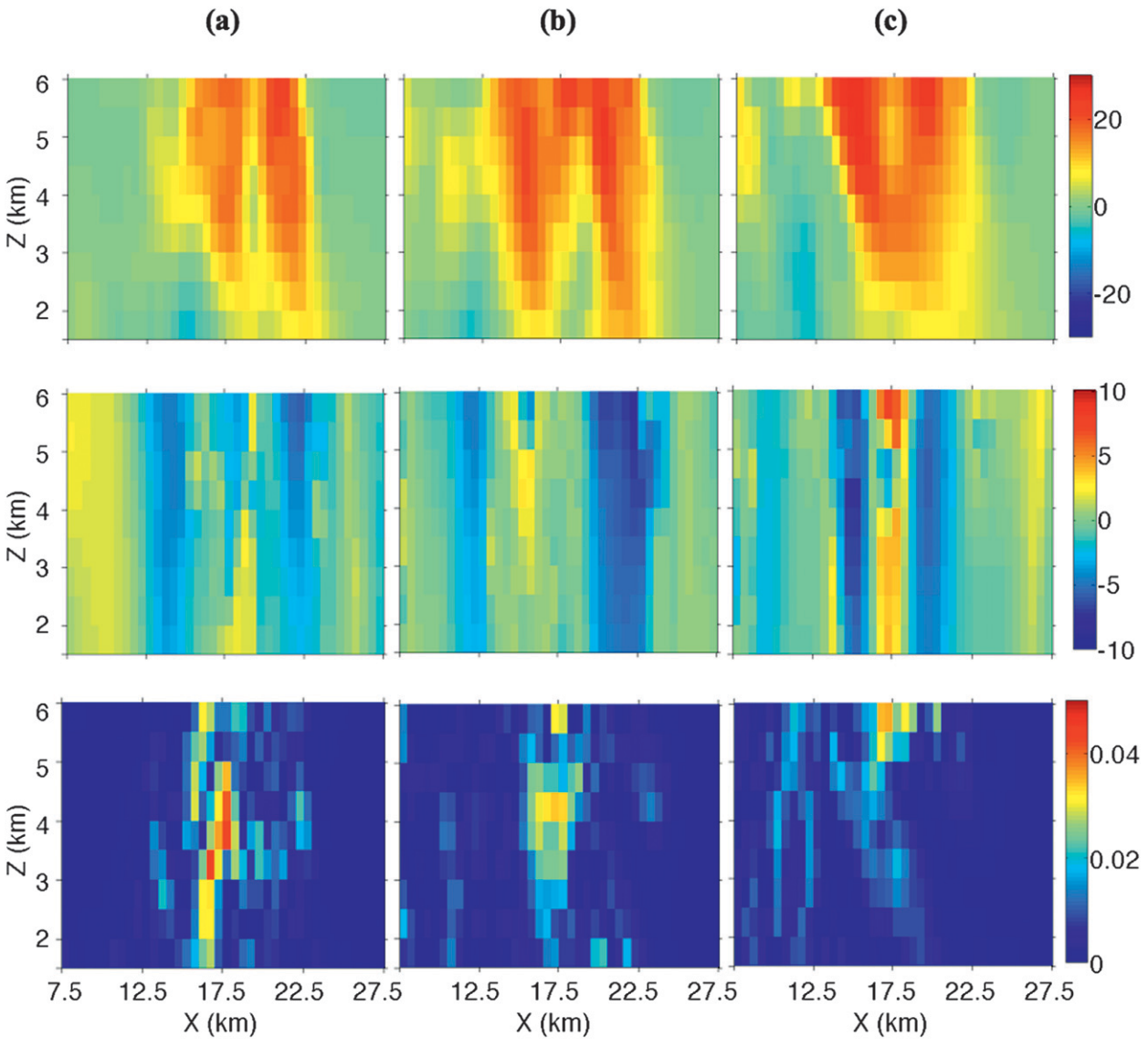

FIG. 8. Vertical cross sections of (top) ARPS upscaled w, (middle) the w^a error reduction in VORT-adv vs NOVORT, and (bottom) ARPS upscaled $|\zeta|$, valid at (a) $y = 7$ km, (b) $y = 9$ km, and (c) $y = 11$ km.

e. Impact of spatially variable advection correction

The VORT-adv retrievals with the 1.5-km data cutoff height were repeated using horizontally uniform U, V fields. The U, V were obtained for each T and analysis level by applying the iterative reflectivity-based Gal-Chen (1982) advection velocity retrieval method. These modified U, V were used in both the data and vorticity constraints. The effect of using horizontally uniform rather than spatially variable advection correction degraded the w^a by up to 6%, 5%, 2%, and 3% for $T = 30$ s, 1 min, 2 min, and 5 min, respectively. Thus, the spatially variable nature of the advection velocity retrieval procedure added value to the dual-Doppler analyses. That the improvement gained by using spatially variable rather than horizontally uniform U, V generally decreases as T increases is likely due to the corresponding growth in temporal discretization errors.

f. Impact of correcting for flow unsteadiness in the data constraint in VORT experiments

In a final set of experiments the impact of accounting for flow unsteadiness in the data constraint was revisited (see section 3c), but VORT retrievals were used. We remind the reader that in the default VORT experiment, advection, but not intrinsic evolution, was accounted for in the data constraint. In this section, the results of three

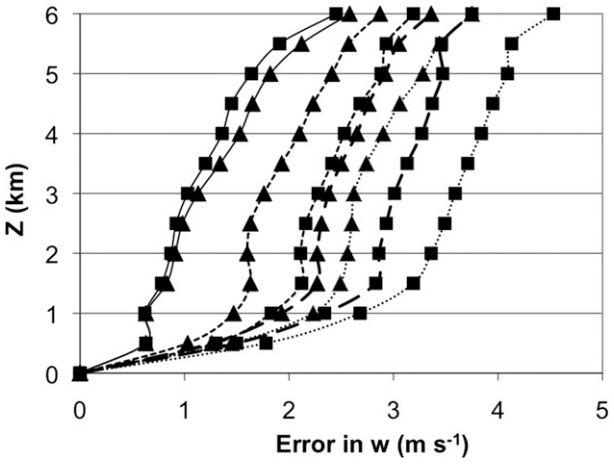

FIG. 9. The RMS w^a errors in the $T = 2$ min VORT (triangles) and NOVORT (squares) retrievals with no data cutoff (i.e., CONTROL; solid curves) or with data cutoff heights of 1.5 km (dotted curves), 1.0 km (long-dashed curves), and 0.5 km (short-dashed curves).

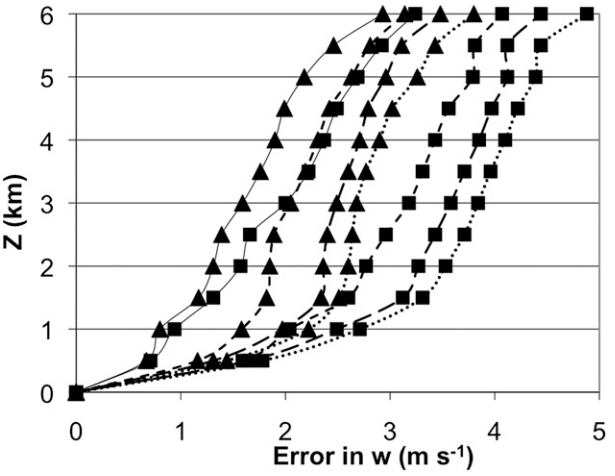

FIG. 10. As in Fig. 9, but for analyses in which radial wind data are omitted where reflectivity <5 dBZ.

experiments are compared to that experiment: VORT-E (only evolution accounted for), VORT-AE (both advection and evolution accounted for), and VORT-N (neither effect accounted for). As in the previous VORT retrievals, advection and intrinsic evolution are accounted for in the vorticity constraint in all of these experiments.

Correcting for advection and/or evolution in the data constraint in the VORT experiments had very similar impacts on u^a, v^a as in the NOVORT and CONTROL experiments. Accordingly, the default VORT retrieval produced the smallest errors in u^a, v^a (not shown). However, the default VORT experiment did not generally produce the best w^a retrievals (Fig. 11). The w^a errors in VORT-N decreased (relative to the default VORT retrievals) for $T = 30$ s and $T = 2$ min, respectively, and increased for $T = 5$ min. The w^a errors in VORT-E and VORT-AE decreased for all three T. Thus, unlike in the CONTROL and NOVORT experiments, using evolution correction in the data constraint in the VORT experiments tended to improve the retrieval of w^a (but, as in the CONTROL and NOVORT experiments, slightly increased the u^a, v^a errors).

4. Experiments with 8 May 2003 Oklahoma supercell radar data

a. Experimental setup and verification

The impact of the vorticity constraint was next explored using real Doppler radar observations of a tornadic supercell that passed over central Oklahoma on 8 May 2003. Data were collected by KTLX, a WSR-88D radar at Twin Lakes near Oklahoma City, and KOKC, a Terminal Doppler Weather Radar located ~25 km west-southwest of KTLX. The most relevant sampling characteristics of the radars are given in Table 1. Because of the shallowness of the sampled elevation angles and the correspondingly small contribution of w_t to the radial wind observations, we did not attempt to account for falling hydrometeors in our analyses. The provisional retrievals proceeded on a 30 km × 30 km × 3 km domain and the final dual-Doppler analyses on a 20 km × 20 km × 3 km domain (Fig. 12). Both domains had 500-m grid spacing. We terminated our analyses at $z = 3$ km because dual-Doppler coverage decreased rapidly at higher levels resulting from large regions of missing KOKC data. The Cressman radius used to interpolate observations to the analysis grid was set to 1 km to account for the large vertical gaps between successive KOKC plan position indicator (PPI) scans.

All of the radar data were manually edited using the National Center for Atmospheric Research (NCAR) SOLO II software (Oye et al. 1995). The U, V used in the provisional and final retrievals were obtained on a 60 km × 60 km domain with 500-m grid spacing using $\beta = 400$ dBZ^2 and $\Delta t \approx 15$ s. The reflectivity CAPPIs used to retrieve U, V were analyzed from three consecutive KTLX volume scans valid at 2225:31–2229:38, 2230:28–2234:36, and 2235:26–2239:32 UTC ($T \approx 5$ min). The CAPPIs were created using the NCAR REORDER software (Oye and Case 1995) with 3D Cressman interpolation (cutoff radius = 750 m). The U and V were generally 10–20 and ~10 m s^{-1}, respectively, and were qualitatively consistent with the displacement of the reflectivity field between successive PPI scans. The dual-Doppler analyses presented below are valid at the beginning of the first KTLX base velocity scan (2225:51 UTC). The

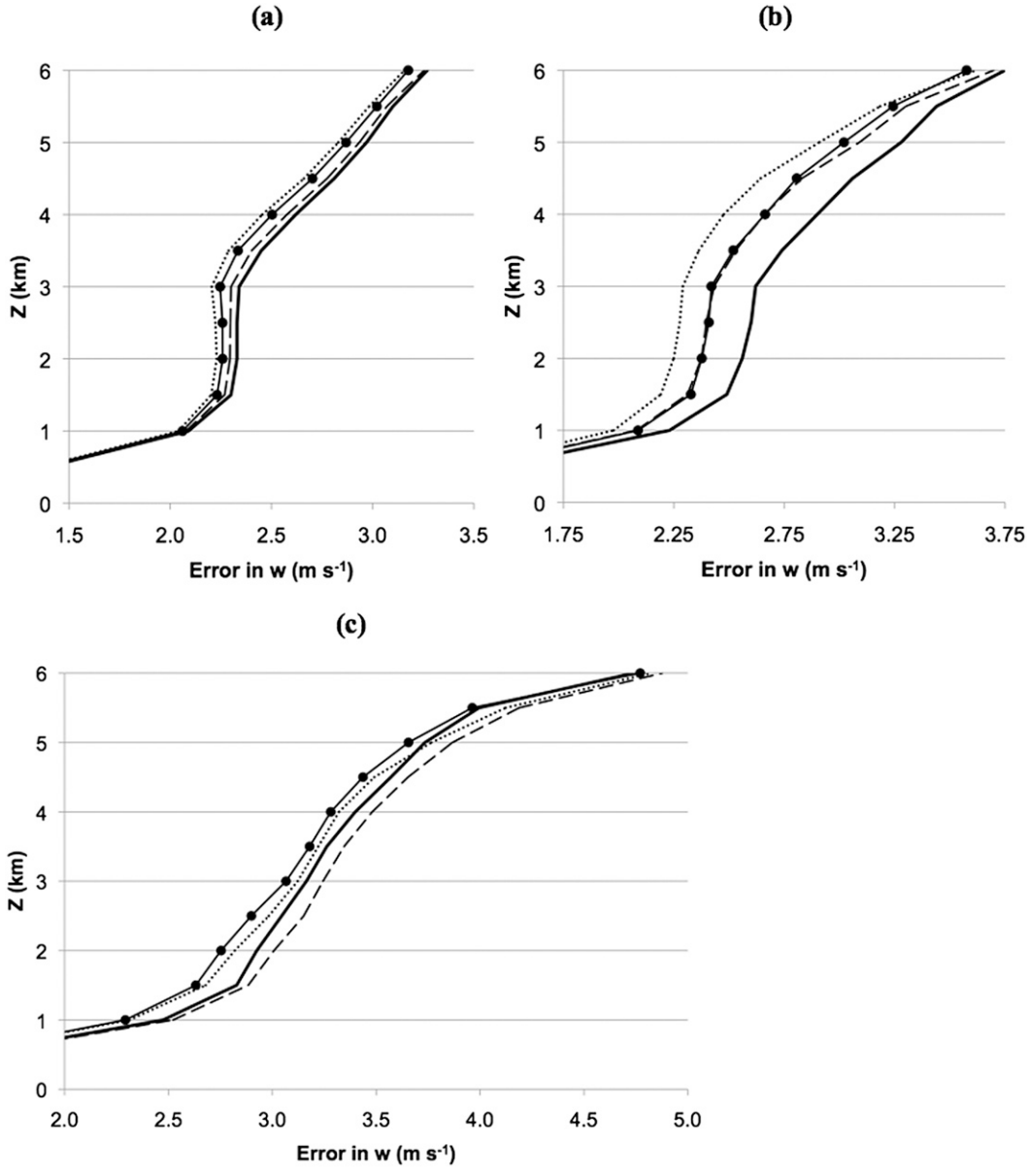

FIG. 11. The RMS w^a errors in VORT (plain), VORT-N (dashed), VORT-E (dotted), and VORT-AE (circles) for T = (a) 30 s, (b) 2 min, and (c) 5 min.

provisional retrievals from which $D\zeta/Dt$ was calculated are valid at the beginnings of the base velocity scans from the first and second KTLX volume scans, that is, 2225:51 and 2230:47 UTC.

As in the ARPS experiments, these real data experiments focus on the value added by the vorticity constraint when low-level radar data are lacking. Accordingly, we present results of NOVORT and VORT retrievals with

TABLE 1. Sampling characteristics of radars in 8 May 2003 experiments.

Radar	T	Azimuthal increment	Range increments (velocity/reflectivity)	Elevation angles (°)
KTLX	~5 min	~1°	250 m/1000 m	0.5, 1.5, 2.4, 3.3, 4.3, 5.2, 6.2, 7.5, 8.7, 10.0, 12.0, 14.0
KOKC	~4 min	~1°	150 m/150 m	0.5, 2.5, 5.1, 7.7, 11.3, 15.3

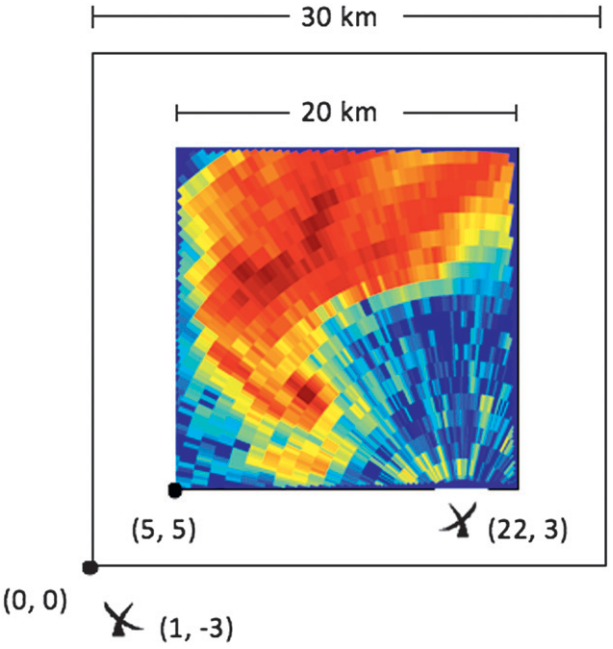

FIG. 12. The provisional and final analysis domains and relative radar locations in the 8 May 2003 experiments. The portion of the 2225:31 UTC KTLX base reflectivity PPI located within the final analysis domain is shown.

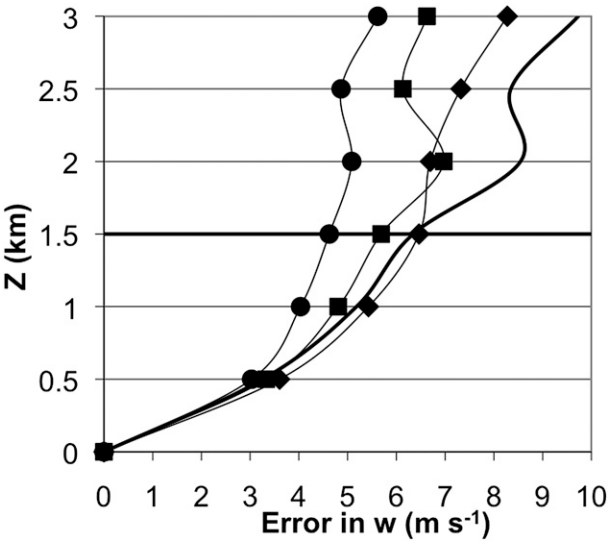

FIG. 13. The RMS CONTROL w (plain curve) and RMS w^a errors in NOVORT (squares), VORT-adv (circles), and VORT-neither (diamonds). The bold horizontal line represents the 1.5-km data cutoff height.

observations in both experiments omitted below a 1.5-km data cutoff height. As in the previous section, no data cutoff is imposed in CONTROL.

Because the true 3D wind fields are not known, verification of the retrievals in this case is more problematic than in the ARPS experiments. Fortunately, because the storm was in close proximity to the radars and high-quality velocity data were available down to the lowest PPI scans (0.5°), a dual-Doppler analysis using all of the available radar data would incorporate much information about the low-level divergence field that is not provided to NOVORT and VORT. Accordingly, we use the CONTROL analysis to verify the NOVORT and VORT retrievals.

In preliminary experiments, setting the (tunable) constraint weighting parameters to those used in the ARPS retrievals produced excessively noisy analyses. We attribute this to the emulated radial velocity fields in the ARPS experiments (obtained from winds that were Cressman interpolated from the 25-m ARPS grid to the spherical radar grid) being visibly smoother than the Doppler velocity fields in the real data experiments. The default smoothness weighting parameter was subsequently increased ($C_s = 10^{-2}$) in the experiments below. The vorticity constraint parameter C_V was also increased (to 10^{-3}) in these experiments; the sensitivity of w^a to C_V is examined later.

b. Impact of vorticity constraint

In this section, we explore the impact of the vorticity constraint and the accounting for wind field advection and/or evolution in the local vorticity derivative (Fig. 13). Consistent with the ARPS experiments with the same volume scan time ($T = 5$ min), the w^a errors in VORT-adv were substantially reduced from both NOVORT and VORT-neither. The mesocyclonic updraft, the enhanced downdraft region located northwest of it, and the updraft atop the rear-flank gust front (near the southeast corner of the analysis domain) were all visibly better analyzed in VORT-adv than in NOVORT (Fig. 14). The differences between VORT-adv and VORT-neither were larger than in the ARPS experiments, consistent with the larger U, V in the present case. The VORT w^a (errors not shown) differed by less than 1% from the VORT-adv w^a. That the vorticity evolution correction in VORT did not improve w^a is not surprising given the large volume scan time and its consistency with the ARPS experiments.

A set of experiments was performed (Fig. 15) to assess the sensitivity of the VORT-adv w^a to C_V (the remaining weighting parameters were set to their default values). The tested C_V ranged over a factor of 100 and included that used in the ARPS experiments ($C_V = 10^{-4}$). Fortunately, the VORT-adv w^a was superior to the NOVORT w^a in all cases. These results suggest the improvement gained by the vorticity constraint is not unduly sensitive to the selected C_V.

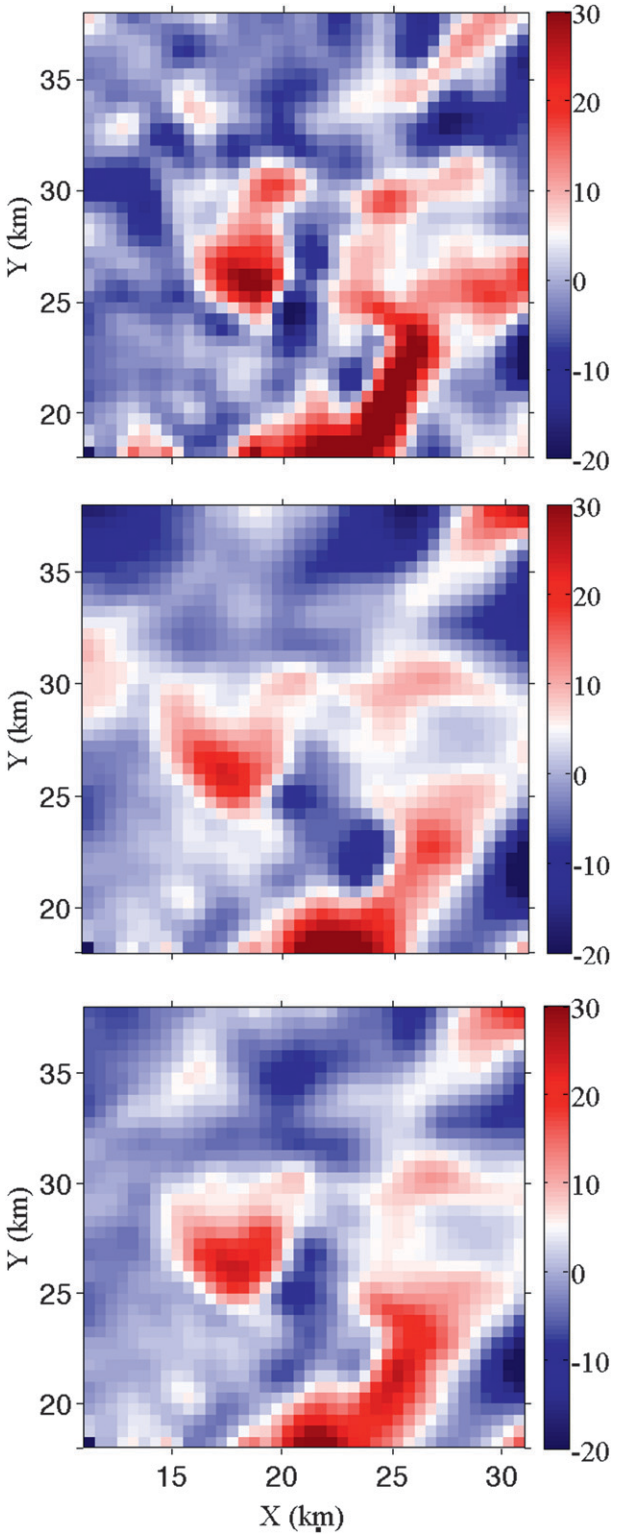

FIG. 14. (top) CONTROL w^a, (middle) NOVORT w^a, and (bottom) VORT-adv w^a valid at 2225:51 UTC and $z = 2.0$ km.

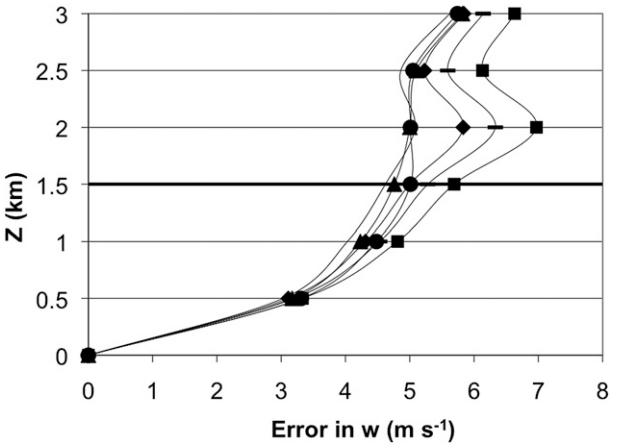

FIG. 15. The RMS w^a errors (valid at 2225:51 UTC) in NOVORT (squares) and VORT-adv with $C_V = 10^{-4}$ (dashes), $C_V = 3 \times 10^{-4}$ (diamonds), $C_V = 10^{-3}$ (plain curve), $C_V = 3 \times 10^{-3}$ (triangles), and $C_V = 10^{-2}$ (circles). The bold horizontal line represents the 1.5-km data cutoff height.

5. Summary

A longstanding problem in radar meteorology is the retrieval of the vertical wind w in convective storms from dual-Doppler data. We have demonstrated that imposing a vertical vorticity equation constraint can substantially improve dual-Doppler retrievals of w in supercell thunderstorms, particularly when low-level radar coverage is lacking. Our use of a high-resolution ARPS supercell simulation allowed us to rigorously explore the impact of the vorticity constraint in a quasi-realistic case. Tests were then performed using real WSR-88D and TDWR radar data of a supercell that traversed central Oklahoma on 8 May 2003.

In the ARPS experiments, including the vorticity constraint in retrievals with pseudo-observations omitted below 1.5 km improved the w analysis for all volume scan times ($T = 30$ s to 5 min). The vorticity constraint also improved w retrievals when no data cutoff height was imposed but radial velocity data were omitted in weak reflectivity regions. This implies that the vorticity constraint can be valuable even when the radars scan very close to the ground. In both sets of experiments, the largest improvements occurred with the shorter volume scan times. This suggests that a vorticity constraint may be especially valuable to dual-Doppler analyses of data from rapidly scanning radars such as phased array weather radars (Zrnic et al. 2007), Doppler on Wheels radars (Wurman et al. 1997), and those developed by the Engineering Research Center for the Collaborative Adaptive Sensing of the Atmosphere (CASA; Brotzge et al. 2010). Accounting for wind field advection in the data and vorticity constraints improved the retrieved w for all volume

scan times. Moreover, superior w analyses were obtained using horizontally variable rather than horizontally uniform pattern translation components. Accounting for intrinsic evolution of the wind field in the vorticity constraint improved the retrieved w for shorter volume scan times (e.g., $T = 30$ s and 1 min). However, the benefit decreased with increasing T, and the analysis was actually slightly degraded for $T = 5$ min.

In the experiments with real radar data of a supercell, the vorticity constraint again improved the retrievals. This is especially encouraging given the large time interval (5 min) between successive volume scans in that case. As in the $T = 5$ min ARPS experiments, the retrieved w was negligibly impacted by vorticity evolution correction (likely in part due to errors in the vorticity evolution estimates), but was substantially improved by accounting for wind field advection.

One valuable extension of this work would be to use Observing System Simulation Experiments (OSSEs) to explore the effects of varying the spatial radar sampling characteristics (e.g., distance from radar, azimuthal sampling interval, cross-beam angle). A more general assessment of the impact of the vorticity constraint could also be gained by testing the technique with additional real storms, including nonsupercells, particularly in cases where high-resolution radar observations extending very close to the ground permit rigorous verification. It would be especially interesting to assess the improvement from the vorticity constraint in real data cases with relatively short (<2 min) volume scan times.

Acknowledgments. This research was largely supported by the National Science Foundation (NSF) under Grant ATM-0532107. Part of the work was performed while the first author held a National Research Council Research Associateship Award at the National Severe Storms Laboratory (NSSL). Partial support of this work was provided by the NSSL. The authors were also supported by NSF Grant EEC-0313747, and the third author was also supported by NSF Grants AGS-0802888, OCI-0905040, and AGS-0750790. The SOLO II and REORDER software developed at the National Center for Atmospheric Research (NCAR) were used to edit the radar data. Most of the data editing was performed by Katherine Willingham (NSSL). We are thankful to Daniel Betten (University of Oklahoma) for helpful discussions and to the three anonymous reviewers for their very useful comments.

REFERENCES

Brandes, E. A., 1977: Flow in severe thunderstorms observed by dual-Doppler radar. *Mon. Wea. Rev.,* **105,** 113–120.

Brotzge, J., K. Hondl, B. Philips, L. Lemon, E. J. Bass, D. Rude, and D. L. Andra, 2010: Evaluation of distributed collaborative adaptive sensing for detection of low-level circulations and implications for severe weather warning operations. *Wea. Forecasting,* **25,** 173–189.

Cressman, G. P., 1959: An operational objective analysis system. *Mon. Wea. Rev.,* **87,** 367–374.

Gal-Chen, T., 1982: Errors in fixed and moving frames of reference: Applications for conventional and Doppler radar analysis. *J. Atmos. Sci.,* **39,** 2279–2300.

Gao, J., M. Xue, A. Shapiro, and K. K. Droegemeier, 1999: A variational method for the analysis of three-dimensional wind fields from two Doppler radars. *Mon. Wea. Rev.,* **127,** 2128–2142.

Liou, Y.-C., and Y.-J. Chang, 2009: A variational multiple–Doppler radar three-dimensional wind synthesis method and its impacts on thermodynamic retrieval. *Mon. Wea. Rev.,* **137,** 3992–4010.

Liu, S., C. Qiu, Q. Xu, P. Zhang, J. Gao, and A. Shao, 2005: An improved method for Doppler wind and thermodynamic retrievals. *Adv. Atmos. Sci.,* **22,** 90–102.

——, M. Xue, and Q. Xu, 2007: Using wavelet analysis to detect tornadoes from Doppler radar radial velocity observations. *J. Atmos. Oceanic Technol.,* **24,** 344–359.

May, R. M., M. I. Biggerstaff, and M. Xue, 2007: A Doppler radar emulator with an application to the detectability of tornadic signatures. *J. Atmos. Oceanic Technol.,* **24,** 1973–1996.

Mewes, J. J., and A. Shapiro, 2002: Use of the vorticity equation in dual-Doppler analysis of the vertical velocity field. *J. Atmos. Oceanic Technol.,* **19,** 543–567.

Mohr, C. G., L. J. Miller, R. L. Vaughan, and H. W. Frank, 1986: The merger of mesoscale datasets into a common Cartesian format for efficient and systematic analysis. *J. Atmos. Oceanic Technol.,* **3,** 143–161.

Oye, D., and M. Case, 1995: REORDER: A program for gridding radar data—Installation and use manual for the UNIX version. Atmospheric Technology Division, National Center for Atmospheric Research, 44 pp. [Available online at http://www.eol.ucar.edu/instrumentation/airborne-instruments/eldora/eldora-help-center/manual/reorder-reference-manual/unixreorder.pdf.]

Oye, R., C. Mueller, and S. Smith, 1995: Software for radar translation, visualization, editing, and interpolation. Preprints, *27th Conf. on Radar Meteorology,* Vail, CO, Amer. Meteor. Soc., 359–361.

Potvin, C. K., A. Shapiro, T.-Y. Yu, J. Gao, and M. Xue, 2009: Using a low-order model to detect and characterize tornadoes in multiple-Doppler radar data. *Mon. Wea. Rev.,* **137,** 1230–1249.

Press, W. H., S. A. Teukolsky, W. T. Vetterling, and B. P. Flannery, 1992: *Numerical Recipes in FORTRAN: The Art of Scientific Computing*. 2nd ed. Cambridge University Press, 963 pp.

Protat, A., and I. Zawadzki, 2000: Optimization of dynamic retrievals from a multiple-Doppler radar network. *J. Atmos. Oceanic Technol.,* **17,** 753–760.

——, ——, and A. Caya, 2001: Kinematic and thermodynamic study of a shallow hailstorm sampled by the McGill bistatic multiple-Doppler radar network. *J. Atmos. Sci.,* **58,** 1222–1248.

Ray, P. S., B. Johnson, K. W. Johnson, J. S. Bradberry, J. J. Stephens, K. K. Wagner, R. B. Wilhelmson, and J. B. Klemp, 1981: The morphology of severe tornadic storms on 20 May 1977. *J. Atmos. Sci.,* **38,** 1643–1663.

Shapiro, A., S. Ellis, and J. Shaw, 1995: Single-Doppler velocity retrievals with Phoenix II data: Clear air and microburst wind

retrievals in the planetary boundary layer. *J. Atmos. Sci.,* **52,** 1265–1287.

——, C. K. Potvin, and J. Gao, 2009: Use of a vertical vorticity equation in variational dual-Doppler wind analysis. *J. Atmos. Oceanic Technol.,* **26,** 2089–2106.

——, K. M. Willingham, and C. K. Potvin, 2010a: Spatially variable advection correction of radar data. Part I: Theoretical considerations. *J. Atmos. Sci.,* **67,** 3445–3456.

——, ——, and ——, 2010b: Spatially variable advection correction of radar data. Part II: Test results. *J. Atmos. Sci.,* **67,** 3457–3470.

Taylor, G. I., 1938: The spectrum of turbulence. *Proc. Roy. Soc. London,* **164A,** 476–490.

Tong, M., and M. Xue, 2005: Ensemble Kalman filter assimilation of Doppler radar data with a compressible nonhydrostatic model: OSS experiments. *Mon. Wea. Rev.,* **133,** 1789–1807.

Wurman, J., J. Straka, E. Rasmussen, M. Randall, and A. Zahrai, 1997: Design and deployment of a portable, pencil-beam, pulsed, 3-cm Doppler radar. *J. Atmos. Oceanic Technol.,* **14,** 1502–1512.

Xue, M., K. K. Droegemeier, and V. Wong, 2000: The Advanced Regional Prediction System (ARPS)—A multiscale nonhydrostatic atmospheric simulation and prediction tool. Part I: Model dynamics and verification. *Meteor. Atmos. Phys.,* **75,** 161–193.

——, and Coauthors, 2001: The Advanced Regional Prediction System (ARPS)—A multi-scale nonhydrostatic atmospheric simulation and prediction tool. Part II: Model physics and applications. *Meteor. Atmos. Phys.,* **76,** 143–165.

——, S. Liu, and T.-Y. Yu, 2007: Variational analysis of oversampled dual-Doppler radial velocity data and application to the analysis of tornado circulations. *J. Atmos. Oceanic Technol.,* **24,** 403–414.

Zrnic, D. S., and Coauthors, 2007: Agile-beam phased array radar for weather observations. *Bull. Amer. Meteor. Soc.,* **88,** 1753–1766.